

Comparison of high-order harmonic generation of Ar using truncated Bessel and Gaussian beams

Cheng Jin and C. D. Lin

J. R. Macdonald Laboratory, Physics Department, Kansas State University, Manhattan, Kansas 66506-2604, USA

(Received 3 February 2012; published 22 March 2012)

We study high-order harmonic generation (HHG) spectra by a focused truncated Bessel beam versus a Gaussian beam, including macroscopic propagation of the fundamental laser and harmonic fields in the gas medium, with the single-atom-induced dipole response calculated from the recently developed quantitative rescattering theory. We first simulate the HHG spectra of Ar by an 8-fs and 780-nm short laser pulse, reported by Wörner *et al.* [*Phys. Rev. Lett.* **102**, 103901 (2009)], assuming the incident beam is a truncated Bessel beam or a Gaussian beam. Both simulations fail to reproduce the observed wide and deep Cooper minimum in the HHG spectra. However, we are able to reproduce the HHG spectra of Ar generated by few-cycle 1800-nm near-infrared lasers, reported recently by Shiner *et al.* [*Nature Phys.* **7**, 464 (2011)]. We also provide a systematic phase-mismatch analysis in the gas jet to examine the spatial growth of harmonics for tight-focusing versus loose-focusing lasers. The dependence of phase mismatch on the gas-jet position and gas pressure is investigated. Finally, we check the divergence of the harmonic beam generated by a tight-focusing versus loose-focusing truncated Bessel beam. These studies show that for a typical gas-jet experiment, whether the spatial mode is a truncated Bessel beam or a Gaussian beam is important only when the laser beam is tightly focused.

DOI: [10.1103/PhysRevA.85.033423](https://doi.org/10.1103/PhysRevA.85.033423)

PACS number(s): 32.80.Rm, 42.65.Ky, 31.70.Hq, 32.80.Fb

I. INTRODUCTION

High-order harmonic generation (HHG) has been widely studied for more than two decades for its potential as a short-wavelength light source [1,2], and for the production of ultrashort attosecond pulses [3–5]. HHG by a single atom is well described qualitatively in terms of the three-step model [6–8], but a full quantitative description of HHG in a macroscopic medium requires the inclusion of the propagation of the fundamental laser field and the generated harmonic field. Recently, our group developed a quantitative rescattering (QRS) theory that can calculate the single-atom (or single-molecule) response [9–11] efficiently. This theory was subsequently corroborated in the analytical form by Frolov *et al.* [12,13]. The QRS theory was further incorporated into the well-established macroscopic propagation theory by Jin *et al.* [14,15] such that the simulated HHG spectra can be compared directly with experimental measurements. So far we have successfully simulated the HHG spectra that have been reported in targets such as Ar [15,16], N₂ [16,17], and CO₂ [18], where experimental conditions have been well specified. The harmonics in these studies were generated with multicycle (FWHM, ~ 10 optical cycles) laser pulses. Later on, we simulated the HHG spectra of Xe by few-cycle (~ 2 optical cycles) mid-infrared lasers [19,20] and we were able to reproduce the observed harmonic spectra. We also made an investigation of the harmonics generated in Ar and Ne atoms under the conditions of very high intensities and high pressures, where the nonlinear propagation of the laser field in the medium undergoes severe modifications [21]. All of these simulations were based on the assumption that the initial fundamental laser pulse at the entrance of the gas medium is a Gaussian beam.

Few-cycle pulses are usually obtained by a gas-filled hollow-core fiber compression technique [22]. This method actually produces a truncated Bessel (TB) beam instead of a Gaussian beam. Nisoli *et al.* [23,24] showed that the spatial properties (divergence and brightness) of the harmonics were

greatly improved using a TB beam as the driving laser pulse. A TB beam is also obtained by spatial filtering of a Gaussian pulse in a hollow-core fiber (without filled gas). Bandulet *et al.* [25] measured the total HHG yield over a range of photon energy using such a TB beam and found that the harmonic yield was stronger and had less divergence compared to harmonics generated from a Gaussian beam. In order to simulate harmonics generated by few-cycle pulses, we generalize our propagation code to include situations where the spatial distribution of the generating laser pulse is a TB beam.

Our goals in this paper are twofold. First, using the spatial TB beam, we want to see if we can simulate the high-harmonic spectra of Ar reported by Wörner *et al.* [26], which were carried out with a few-cycle laser at relatively high intensities (Fig. 1 of their paper). We have not been able to reproduce these spectra by assuming a spatial Gaussian beam. Our second goal is to establish the conditions where the generated harmonic spectra are insensitive to whether the generating beam is a Gaussian or a TB beam for a typical gas-jet experiment.

An in-depth detailed HHG theory with the inclusion of the macroscopic propagation of the fundamental and harmonic fields where the single-atom harmonics are obtained by the QRS theory has been given in Ref. [15]. We modify the numerical code by changing the initial condition in which the input beam is a TB beam. A TB beam exiting from the hollow-core fiber is usually refocused through lenses and mirrors before entering the harmonic-generating gas medium. In Appendix A, we describe two types of TB beams. In TB-1 (Type-1 Bessel), a tight-focusing beam was used by Nisoli *et al.* [23,24]. In TB-2 (Type-2 Bessel), a loosely focused TB beam was used by Wörner *et al.* [26] and Shiner *et al.* [27]. In Sec. II, we show the calculated HHG spectra of Ar with a TB beam or a Gaussian beam using a 780-nm laser and setup parameters as close as those in Wörner *et al.* [26]. Even with the TB-2 beam, we still have not been able to reproduce the observed deep Cooper minimum (CM) reported in the experiment. However, we are able to

reproduce the HHG spectra of Ar reported in Shiner *et al.* [27], where the harmonic spectra were generated using 1800-nm mid-infrared lasers. In Sec. III, we turn to study the detailed harmonic growth maps in space for TB-1 and TB-2 beams. Specifically, we investigate how these maps change with the gas-jet position and gas pressure in terms of phase-matching conditions. We also check the divergence of harmonics generated by TB-1 and TB-2 beams. We then draw the conclusion that for a TB-2 beam, the HHG spectra are generally close to those generated from a Gaussian beam with the similar beam waist. A summary in Sec. IV concludes this paper. For completeness, Appendix A summarizes the basics of TB-1 and TB-2 beams. Appendix B gives a summary of the different terms that contribute to phase mismatch in a gas medium.

II. SIMULATION OF EXPERIMENTAL HARMONIC SPECTRA OF Ar

A. HHG spectra using a 780-nm laser

High-harmonic spectra of Ar have been widely studied over the years. According to the QRS theory, the HHG spectra generated from a single atom would mimic the field-free photoionization cross section of the atom. Following the works of Refs. [14–16], it has been further established that the macroscopic HHG spectra can be written as

$$S_h(\omega) \propto |W(\omega)|^2 \sigma^R(\omega), \quad (1)$$

where $W(\omega)$ is the “macroscopic wave packet” (MWP), and $\sigma^R(\omega)$ is the differential photorecombination cross section (PRCS). The $\sigma^R(\omega)$ is related to photorecombination transition dipole $d(\omega)$ by

$$\sigma^R(\omega) \propto \frac{\omega^3}{p} |d(\omega)|^2, \quad (2)$$

where p is the momentum of the continuum electron. It is well known that the photoionization cross section (PICS) of Ar has a minimum [28], called the Cooper minimum (CM), at photon energy near 51 eV. The Cooper minimum also appears in the harmonic spectra of Ar, and has been reported in many measurements [16,26,27,29–33] using different laser intensities and different wavelengths, but the position of the minimum differs somewhat from one experiment to another. To observe a clear CM, the cutoff of the HHG spectrum should lie well above 51 eV. Since the HHG cutoff is given by $I_p + 3.17U_p$, where I_p is the ionization energy and U_p is the ponderomotive energy, in experiments with typical 800-nm Ti:sapphire lasers, this would require a high laser intensity. On the other hand, at high intensities, saturation occurs. Thus, in earlier experiments with 800-nm Ti:sapphire lasers, the CM in the HHG spectrum of Ar was not clearly located. To avoid the saturation effect, in Wörner *et al.* [26] few-cycle laser pulses were used and a clear CM has been reported. In this experiment, a hollow-core fiber filled with Ar gas was used to achieve self-phase modulation for the laser pulse; subsequently, using chirped mirrors, it was compressed to

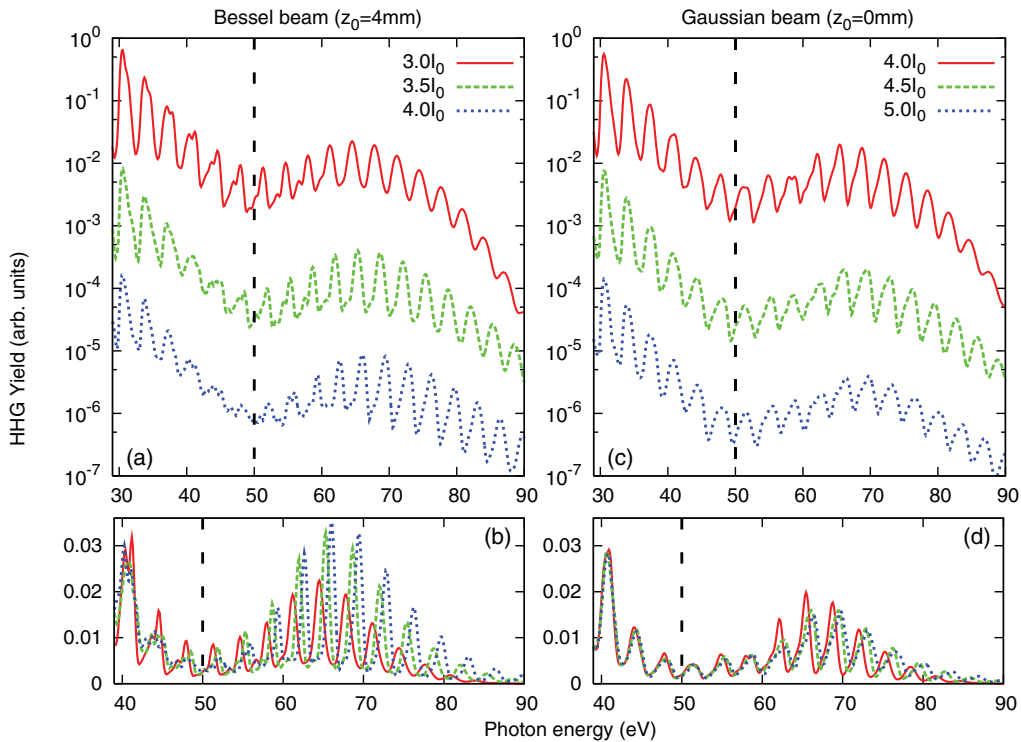


FIG. 1. (Color online) Calculated HHG spectra (CEP averaged) of Ar assuming the initial laser pulse is (a),(b) a truncated Bessel beam (Type 2 in Fig. 15) or (c),(d) a Gaussian beam (beam waist $w_0 = 50 \mu\text{m}$). z_0 is the position of the gas jet with respect to the laser focus, and the laser intensity (at the focus, $z = 0 \text{ mm}$) is given in units of $I_0 = 10^{14} \text{ W/cm}^2$. Dashed lines indicate the position of the Cooper minimum. The laser wavelength is 780 nm. See text for additional laser parameters. This figure should be compared with Fig. 1 in Ref. [26] and Fig. 2(b) below.

a few-cycle pulse (~ 3 optical cycles). The most prominent feature of the experimental result is the appearance of a clear deep CM at 53 ± 3 eV, which does not shift with the laser intensity. The experimental result of Wörner *et al.* [26] appears to be consistent with the general prediction of the QRS, in that the position of the CM is at about 51 eV, and the position does not change with the laser intensity. However, the width and depth of the CM appear to be inconsistent with the prediction of the QRS. (The CM observed in the PICS of Ar is not as deep [28].) We carried out simulations with experimental parameters by assuming that the incident laser pulses were Gaussian beams, but were unable to reproduce the broad and deep Cooper minimum reported in the experiment. We thus decided to investigate whether the limitation is due to the use of a Gaussian beam in the simulation. Here we report the results from simulations using a truncated Bessel beam.

To simulate the measurements, we carry out the macroscopic propagation calculation [15] where the single-atom response is obtained using the QRS theory. In Fig. 1, we show the simulated HHG spectra of Ar. In the calculation, the laser wavelength is 780 nm, and the duration is 3 cycles (FWHM). The gas jet is 1-mm wide in the interaction region, the gas pressure is assumed to be a constant at 30 Torr, and a slit with a width of $100 \mu\text{m}$ is placed at 24 cm after the gas jet to select the harmonics in the far field. These parameters are close to those in Wörner *et al.* [26]. The laser peak intensity at the focus (in the vacuum) is adjusted as indicated in Fig. 1 to obtain the correct experimental cutoff position.

We first assume that the laser pulse is a Gaussian beam with waist $w_0 = 50 \mu\text{m}$ and the center of the gas jet is at the laser focus ($z_0 = 0$ mm). The HHG spectra after being carrier-envelope-phase (CEP) averaged are shown in Fig. 1(c). For clarity, the spectra have been shifted for different intensities. In Fig. 1(d), we show the spectra for three intensities in a linear scale. The CM appears at about 50 eV. Beyond $4 \times 10^{14} \text{ W/cm}^2$, the laser field reaches saturation and higher harmonics show a blue shift. The ratio of the maximum yield near the cutoff with respect to the lowest yield at the CM is about a factor of 3–6 in the simulation, but the same ratio is close to 100 in the experiment of Wörner *et al.* [26] [also see Fig. 2(b) below]. We varied the position of the gas jet (z_0) with respect to the laser focus, but the harmonic spectra remain nearly the same as those in Fig. 1(c).

We next assume that the incident beam is a TB-2 pulse, and the center of the gas jet is located at 4 mm after the laser focus (i.e., $z_0 = 4$ mm). The HHG spectra after being CEP averaged are shown in Figs. 1(a) and 1(b). The laser intensities indicated are the ones at the laser focus ($z = 0$ mm), so the on-axis intensities at $z = 4$ mm are almost the same as those in the Gaussian pulses (at $z = 0$ mm) in Fig. 1(c). The high-harmonic spectra shown in Fig. 1(a) do not differ significantly from those in Fig. 1(c), with the CM appearing near 50 eV. From Fig. 1(b), we find that with the TB-2 beam, the HHG spectra are stronger for the higher harmonics, such that the previous maximum/minimum ratio rises by about 50%, but still much smaller than the ratio seen in Wörner *et al.* [26]. We also changed z_0 (not shown); the CM was always seen, but the depth of the CM reported in the experiment still could

not be reproduced. Thus the origin of the discrepancy remains unexplained.

B. HHG spectra using an 1800-nm laser

Since the ponderomotive energy is proportional to the square of the wavelength of the driving laser, it is preferable to study the CM in the HHG spectra of Ar using near-infrared (NIR) lasers. Indeed, such measurements have been reported by Jin *et al.* [16] using 1.2- and 1.36- μm lasers and by Higuert *et al.* [33] with 1.8- to 2.0- μm and 50-fs NIR lasers. None of these experiments reported the CM as deep as shown in Wörner *et al.* [26]. In fact, the experimental data reported in Jin *et al.* [16] were well reproduced by our simulations using an incident Gaussian beam spatially. Note that Ar HHG spectra generated using long laser pulses in Jin *et al.* [16] were taken with exactly the same experimental chamber as those in Wörner *et al.* [26], (i.e., the gas jet, spectrometer, detector, geometries, etc., were exactly the same in the two experiments). Recently, Shiner *et al.* [27] also reported the measurements of Ar HHG spectra using a few-cycle (~ 2 optical cycles) 1800-nm laser (see Fig. 9 in the supplementary information of Ref. [27]). We show their experimental spectrum in Fig. 2(a). We carry out the simulation with an 1800-nm, 11-fs laser pulse. A gas jet (0.5-mm wide) is located at the

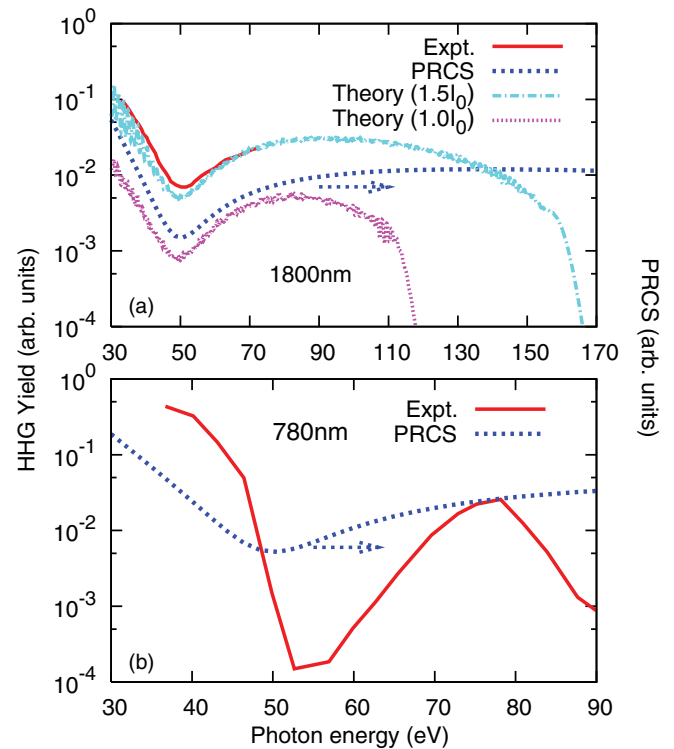


FIG. 2. (Color online) (a) Comparison of experimental (envelope only) [27] and theoretical HHG spectra using an 1800-nm laser. The laser intensity used in the simulation is indicated in units of $I_0 = 10^{14} \text{ W/cm}^2$. See text for additional parameters. The experimental data are shown only from 30 to 75 eV due to constraint from the filter. (b) Experimental HHG spectra (envelope only) [26] using a 780-nm laser with intensity of $2.9 \times 10^{14} \text{ W/cm}^2$. The calculated photorecombination cross section (PRCS) using the Muller potential [34] is also shown in (a) and (b).

laser focus, the gas pressure is 6 Torr, and a slit with a width of $190 \mu\text{m}$ is placed at 45.5 cm after the gas jet. Only the harmonics after the slit are detected. The initial laser beam is assumed to be a Gaussian one with $w_0 = 100 \mu\text{m}$. The calculated HHG spectra (CEP averaged) with two intensities are shown in Fig. 2(a). We can see that the experimental spectrum agrees very well with the theoretical one (laser intensity is $1.5 \times 10^{14} \text{ W/cm}^2$). These spectra also agree well with the calculated PRCS of Ar using the Muller potential [34]. With decreasing laser intensity, the general spectral shape and the depth of the Cooper minimum do not change much, except that the cutoff position moves to a lower photon energy. This also shows that a Gaussian beam can be used to model the experiment of Shiner *et al.* [27]. In other words, the general HHG spectra obtained from a loose-focusing TB beam and Gaussian beam do not differ significantly.

Based on the above simulations, we conclude that the deep Cooper minimum in the HHG spectra reported in Wörner *et al.* [26] remains unreproduced by simulations. On the other hand, the deep minimum was not observed in other experiments using NIR lasers. Our simulations can reproduce these latter observations. In Wörner *et al.* [26], the laser wavelength is 780 nm and the laser intensity is near the saturation. However, the saturation effect was included in our simulation and no drastic differences were seen between an input Gaussian vs TB-2 pulses. As shown in Fig. 3, the macroscopic wave packet (or returning electron wave packet) is relatively flat in the plateau region. To reproduce the observation of Wörner *et al.* [26], the wave packet has to undergo the change of more than a factor of 20 within about 10–20 eV. We are not aware of any possible effects that can cause such a big change on the MWP. In view of the negative results from our extended theoretical analysis, perhaps additional experiments would help to resolve this discrepancy.

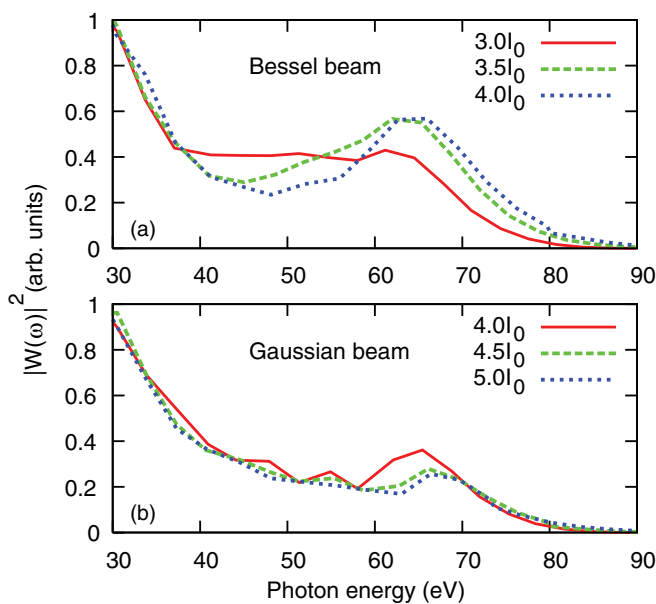


FIG. 3. (Color online) Macroscopic wave packet $|W(\omega)|^2$ defined in Eq. (1) extracted from the harmonic spectra in Fig. 1. Note that linear scales are used to display the wave packets.

III. PHASE-MATCHING CONDITIONS: TRUNCATED BESSEL BEAM VS GAUSSIAN BEAM

In a previous paper, Nisoli *et al.* [23] showed that the characteristics of HHG using a truncated Bessel beam and Gaussian beam were quite different. Our results in Sec. II seem to contradict their conclusions. It turns out that Nisoli *et al.* [23] used a tightly focused truncated Bessel beam (or TB-1), while in Sec. II, a loosely focused truncated Bessel beam (or TB-2) was applied. In Appendix A, we summarize how the two types of TB beams are constructed, together with their typical spatial intensity distributions. In this section, we present a systematic comparison of phase-matching conditions for the TB-1, TB-2, and Gaussian beams. In the calculation, the *ab initio* macroscopic propagation and the QRS theory for the single-atom response are applied, and the laser intensity (at the focus, as shown in Figs. 13 and 15), wavelength, duration (FWHM), and CEP are fixed at $3 \times 10^{14} \text{ W/cm}^2$, 780 nm, 3 cycles, and 0, respectively.

Phase matching is a prerequisite for efficient generation of high harmonics. The phase mismatch for the q th harmonic can be written as [5,35–38]

$$\begin{aligned} \Delta k_q &= (k_q - qk_1) - K_{q,\text{dip}} \\ &= \Delta k_{q,\text{geo}} + \Delta k_{q,\text{el}} + \Delta k_{q,\text{at}} - K_{q,\text{dip}}. \end{aligned} \quad (3)$$

Here the first term of the phase mismatch is due to the geometry of laser focusing. The second term is from the dispersion by free electrons that are present in the gas medium, i.e., free electron or plasma dispersion. The third term is from neutral atom dispersion, where the index of refraction changes with the wavelength. The last term is due to the laser-induced atomic dipole phase, which depends strongly on laser intensity. The dipole-phase mismatch is given by $K_{q,\text{dip}} = \nabla \varphi_{q,\text{dip}}$, where $\varphi_{q,\text{dip}}$ is the action accumulated by an electron during its excursion in the laser field. This phase depends on whether the q th harmonic is emitted by electrons that take the “long” or “short” trajectories. More detailed discussions on these different phase-mismatch terms can be found in Appendix B.

A. Phase-matching map at low gas pressure

We first set the gas pressure very low (0.1 Torr) such that the pressure effect can be ignored. In this case, the phase-matching conditions are only determined by the interplay between the geometric phase, $\varphi_{q,\text{geo}}(r,z) \approx -(q-1)\phi_{\text{laser}}(r,z)$, and the induced dipole phase, $\varphi_{q,\text{dip}}(r,z) = -\alpha_q^2 I(r,z)$, defined in Appendix B. We plot $\Delta\varphi_q(r,z) = \varphi_{q,\text{geo}}(r,z) - \varphi_{q,\text{dip}}(r,z)$, modulo 2π , in Fig. 4 for the 15th harmonic (H15), in contrast to the generally used contour map for the coherence length [37,39]. The color coding is chosen such that it is bright (or white) when $\Delta\varphi_q$ is near π , and dark (or red) when $\Delta\varphi_q$ is near 0 and 2π (such that no color changes at the two boundaries). Note that the length scale is in mm along the z axis and in μm along the r axis. In Fig. 4, the phase between two neighboring white regions is 2π . For good phase matching, this region is large (such that the gradient is small). From the figure, we can see in general that it is easier to achieve good phase matching for short (upper row) rather than for long (lower row) trajectories.

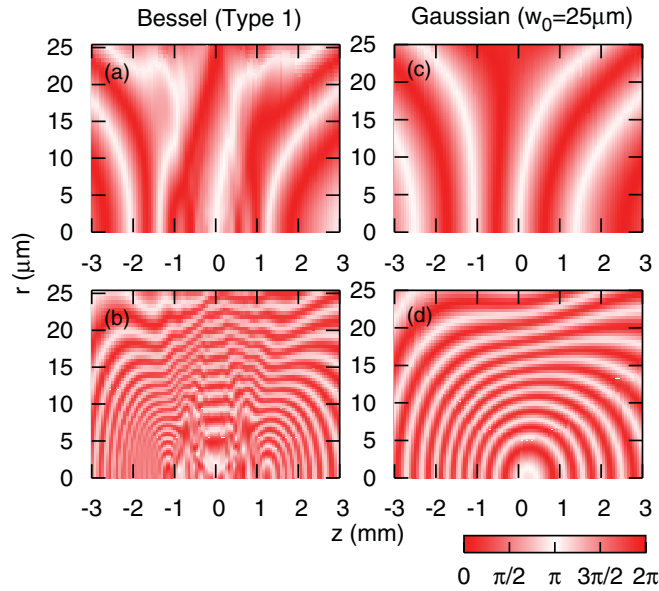


FIG. 4. (Color online) Phase-matching map for H15 of the interplay between the geometric phase $\varphi_{q,\text{geo}}(r,z)$ and induced dipole phase $\varphi_{q,\text{dip}}(r,z)$ for Type-1 Bessel and Gaussian ($w_0 = 25 \mu\text{m}$) beams. Upper row: short trajectory; lower row: long trajectory. Note that $\Delta\varphi_q(r,z) = \varphi_{q,\text{geo}}(r,z) - \varphi_{q,\text{dip}}(r,z)$, modulo 2π , is plotted, and the phase change between two neighboring white regions is 2π .

More explicitly, consider a Gaussian beam where the intensity and phase can be expressed as

$$I(r,z) = \frac{I_0}{1 + (2z/b)^2} \exp \left[- \left(\frac{r}{w_0} \right)^2 \frac{2}{1 + (2z/b)^2} \right], \quad (4)$$

$$\phi_{\text{laser}}(r,z) = -\tan^{-1} \left(\frac{2z}{b} \right) + \frac{k\lambda_1}{2\pi} \left(\frac{r}{w_0} \right)^2 \frac{(2z/b)}{1 + (2z/b)^2}, \quad (5)$$

where the parameters in the above equations are defined in Appendix B. Using the phases in Fig. 4, we can calculate the phase mismatch by taking the gradient. In Figs. 5(c) and 5(d), we show the phase mismatch $\Delta k_q(z)$ for H15 along the propagation axis z for a Gaussian beam. It is much smaller for the short-trajectory component than for the long-trajectory one. Furthermore, phase matching is better after the focus. Since laser intensity decreases quickly away from the focus, a gas jet located at $z = 2 \text{ mm}$ is about near the optimum condition for HHG generation for a Gaussian beam. In Figs. 5(a) and 5(b), the phase mismatch $\Delta k_q(z)$ for a TB beam along the propagation axis z is shown. Again, the phase mismatch is much larger for the long-trajectory component than for the short-trajectory one. Although the phase oscillates widely near $z = 0 \text{ mm}$, the spatial average over a small volume would result in a small phase mismatch. Thus, for TB beams, a broad good phase-matching region close to the axis from $z = -1.5$ to 1.5 mm for short-trajectory harmonics can be achieved. This conclusion is consistent with the experimental results of Nisoli *et al.* [23]. For the typical gas-jet length ($\sim 1 \text{ mm}$), the phase-matching conditions should depend strongly on the position of the gas jet, as well as on whether it is a Type-1 Bessel or Gaussian ($w_0 = 25 \mu\text{m}$) beam.

For harmonics generated away from the axis, the phase mismatch has components parallel and perpendicular to the axis. For a Gaussian beam, the distance between two white regions (where the phase changes by 2π) is larger along the z axis than along the r axis [see Figs. 4(c) and 4(d)], thus phase matching (by taking the gradient of the phase) is still favorable, although not as good as the on-axis region (also see Fig. 4 in Ref. [37]). From Fig. 4, in general, long-trajectory harmonics tend to have off-axis phase matching and the harmonics are more divergent.

We next consider loosely focused laser beams. From Eqs. (4) and (5), we note that for a Gaussian beam, if we scale z by the confocal parameter b , and scale r by the beam waist w_0 , then the intensity and phase stay the same. Thus, for the

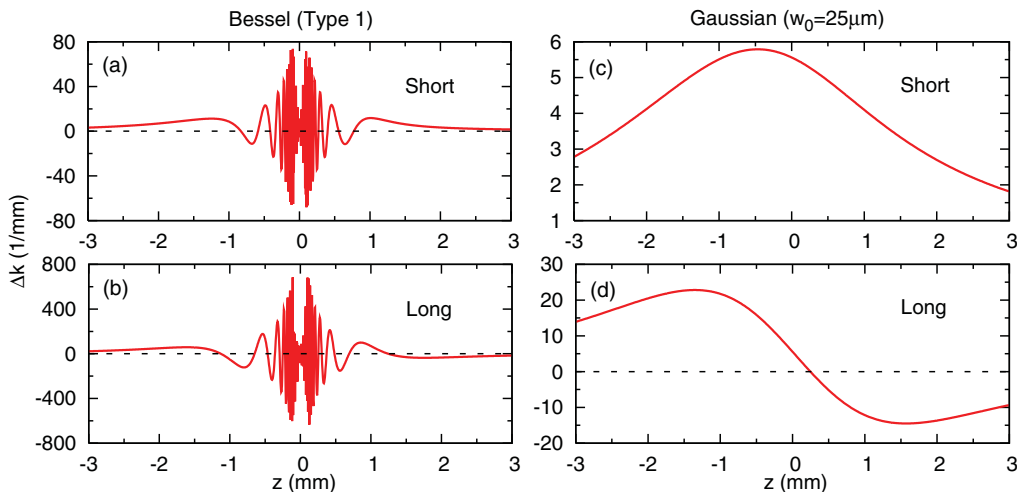


FIG. 5. (Color online) On-axis phase mismatch $\Delta k_q(z) = (\partial/\partial z)[\Delta\varphi_q(0,z)]$ for the phase shown in Fig. 4 with Type-1 Bessel and Gaussian ($w_0 = 25 \mu\text{m}$) beams; $q = 15$. Upper row: short trajectory; lower row: long trajectory. Dashed lines indicate the zero values of the phase mismatch. Note that the values of $\Delta k_q(z)$ from $z = -0.2$ to 0.2 mm in (a) and (b) are probably not precise numerically due to the dramatic phase oscillation along the z direction.

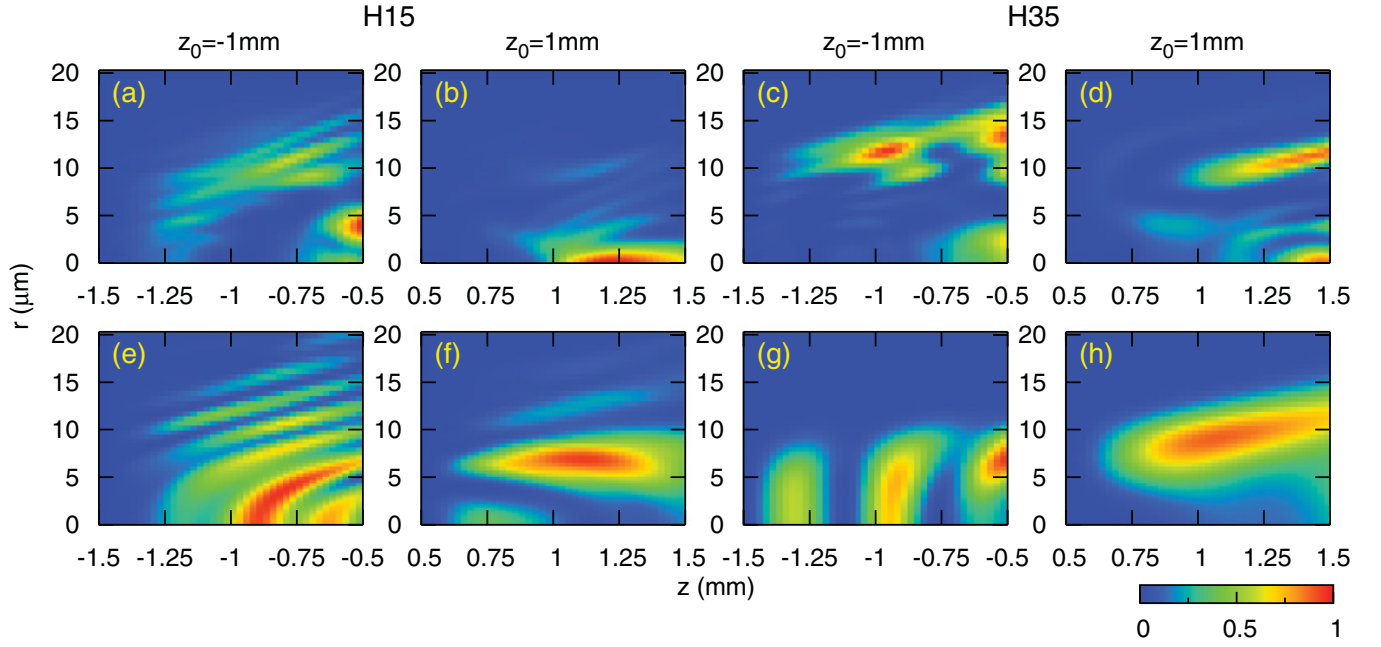


FIG. 6. (Color online) Spatial distributions (normalized) of harmonic intensity for H15 and H35 using tight-focusing laser beams. z_0 is the position of the gas-jet center with respect to the laser focus, i.e., $z_0 > 0$ means the gas jet (1-mm wide) is placed after the laser focus. Gas pressure: 0.1 Torr (i.e., the fundamental laser field is not modified through propagating in the medium). Upper row: Type-1 Bessel beam; lower row: Gaussian beam ($w_0 = 25 \mu\text{m}$).

loosely focused Gaussian beam, the phase-matched volume will increase (by b or w_0 in each direction). For a typical fixed gas-jet length, we expect that good phase-matching conditions are more easily achieved. This is also true for TB beams. We have checked (not shown) that the phase map for TB-2 and Gaussian ($w_0 = 50 \mu\text{m}$) beams were very similar to those shown for TB-1 and Gaussian ($w_0 = 25 \mu\text{m}$) beams in the scaled coordinates (for H15). Thus, for loosely focused TB-2 beams, the phase-matching conditions do not differ much from the loosely focused Gaussian beam. In the next section, we show that in this case, the HHG spectra generated by the TB-2 beam and by the Gaussian beam are very similar.

B. Dependence of harmonic yield on gas-jet position

Figure 6 shows the intensity distributions of the plateau harmonic H15 and cutoff harmonic H35, under tight-focusing conditions at two different gas-jet (1-mm width) positions, for a TB-1 beam and a Gaussian beam. The other laser parameters are given in the figure caption. To understand these results, we examine the phase-mismatch [see Eq. (3)] values in units of 1/mm. In Table I, we show the typical values of $\Delta k_{q,\text{geo}}(0,z) = \nabla \varphi_{q,\text{geo}}(0,z)$ and $K_{q,\text{dip}}(0,z) = \nabla \varphi_{q,\text{dip}}(0,z)$ for a Gaussian

beam at $z = 1 \text{ mm}$ on the axis ($r = 0$). [We caution that the value of $K_{q,\text{dip}}(0,z)$ calculated using α_i^q in the cutoff region in Eq. (B4) may not be very accurate.] Since the gas pressure is very low (0.1 Torr), there is no laser defocusing. For $b = 5 \text{ mm}$ ($w_0 = 25 \mu\text{m}$), as shown clearly in Table I, the short trajectory is favored for good phase matching. The coherence length is $l_{\text{coh}} = \pi/\Delta k_q$, where $\Delta k_q = \Delta k_{q,\text{geo}} - K_{q,\text{dip}}$ is calculated to be about 1 mm for both H15 [also see Figs. 5(c) and 5(d)] and H35. This large coherence length allows the harmonic intensity to grow steadily along the propagation axis z , as seen in Figs. 6(f) and 6(h). If the gas jet is placed before the laser focus ($z_0 = -1 \text{ mm}$), then $K_{q,\text{dip}}$ changes its sign, while $\Delta k_{q,\text{geo}}$ remains the same as that at $z = 1 \text{ mm}$. Thus the coherence length l_{coh} (for either a short or long trajectory) becomes much smaller. In Figs. 6(e) and 6(g), we see that the buildup of the harmonic along z is not monotonic. The small coherence length results in destructive interference such that the harmonic yield vanishes, followed by buildup and then destruction, as z increases. Thus gas-jet position $z_0 = -1 \text{ mm}$ is not favorable for phase matching for the generation of harmonics. For a Type-1 Bessel beam, as shown in Figs. 6(a)–6(d), the harmonic spatial distribution is quite different from the Gaussian beam, but the strong gas-jet

TABLE I. Phase mismatch $\Delta k_{q,\text{geo}}(0,z)$ and $K_{q,\text{dip}}(0,z)$ (mm^{-1}) from Eqs. (B1) and (B4) in Appendix B for a Gaussian beam. Here, $z = 1 \text{ mm}$ and $I_0 = 3 \times 10^{14} \text{ W/cm}^2$.

Harmonic order	H15				H35			
Confocal parameter b (mm)	5	3	20	15	5	3	20	15
$\Delta k_{q,\text{geo}}$	4.83	6.46	1.39	1.83	11.72	15.69	3.37	4.45
$K_{q,\text{dip}}$								
Short (S)	0.71	1.28	0.059	0.103	<9.77	<17.51	<0.81	<1.41
Long (L)	17.12	30.67	1.41	2.47	>9.77	>17.51	>0.81	>1.41

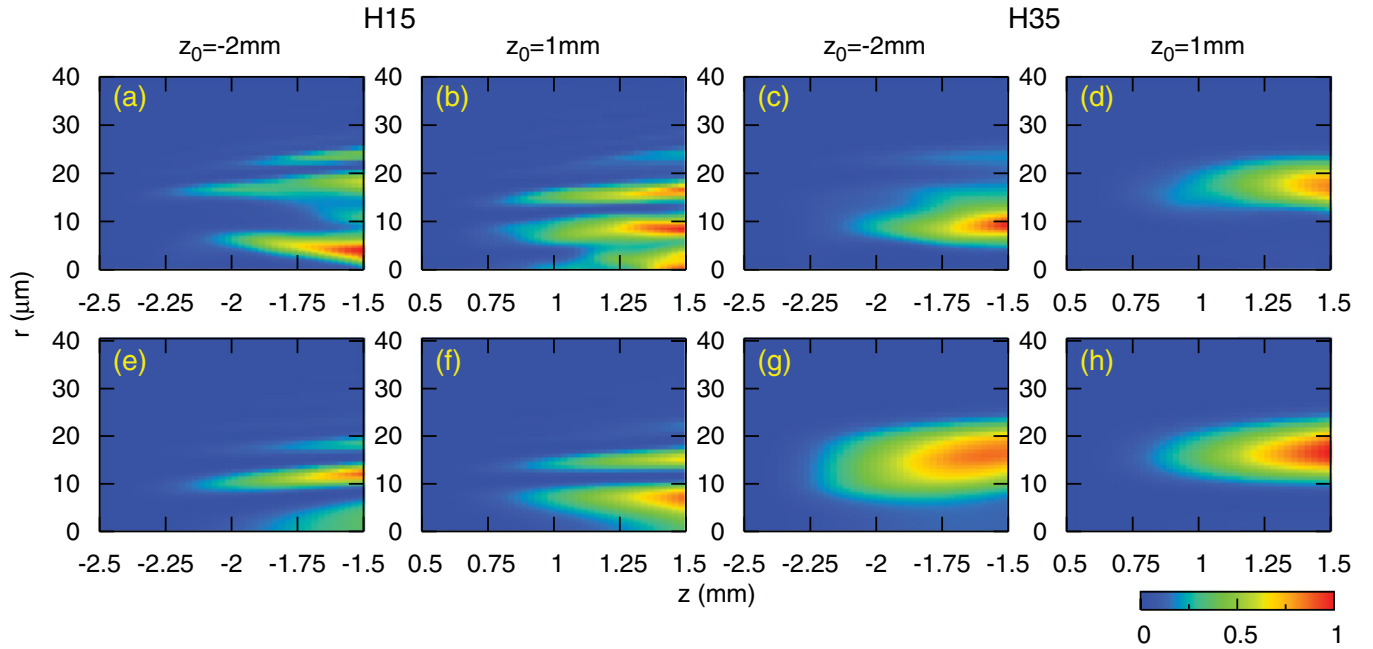


FIG. 7. (Color online) Same as Fig. 6, except for loosely focused laser beams. Upper row: Type-2 Bessel beam; lower row: Gaussian beam ($w_0 = 50 \mu\text{m}$).

position dependence is similar, i.e., the coherence length is shorter for negative z_0 than for positive z_0 .

The same analysis can be done for a loosely focused Gaussian beam ($b = 20 \text{ mm}$, $w_0 = 50 \mu\text{m}$). At $z = 1 \text{ mm}$, l_{coh} is $\sim 2 \text{ mm}$ (H15) or $\sim 1 \text{ mm}$ (H35), and l_{coh} becomes $\sim 1 \text{ mm}$ at $z = -2 \text{ mm}$. The large coherence length allows steadily monotonic buildup of the harmonics as z is increased, as confirmed by numerical results shown in Figs. 7(e)–7(h). For the Type-2 Bessel in Figs. 7(a)–7(d), the harmonic spatial distribution is very similar to the Gaussian beam. These confirm that for loosely focused Gaussian and Bessel beams, the generated harmonic spectra are expected to be quite similar for the same gas-jet positions, and the results are less sensitive to their positions with respect to the laser focus, as discussed in Sec. II.

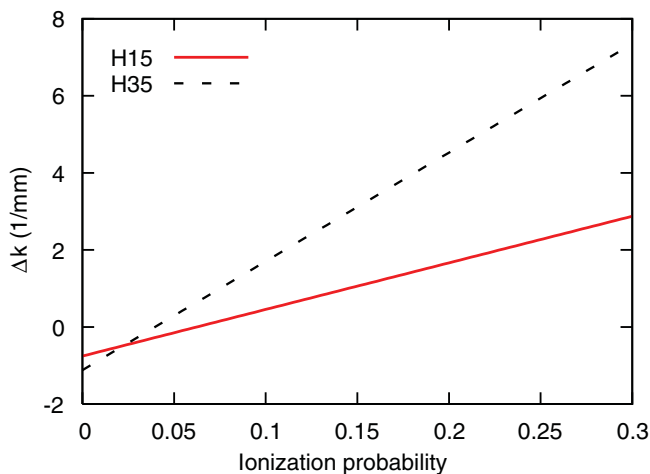


FIG. 8. (Color online) Phase mismatch $\Delta k_{q,el} + \Delta k_{q,at}$ of Ar as a function of ionization probability at the pressure of 10 Torr. This value is proportional to the pressure.

C. Pressure-induced phase mismatch

The phase mismatch $\Delta k_{q,el}$ due to free electrons and $\Delta k_{q,at}$ due to neutral atom dispersion explicitly depend on pressure [40] [also see Eqs. (B6) and (B7)]. In Fig. 8, we plot $\Delta k_{q,el} + \Delta k_{q,at}$ as a function of ionization probability for H15 and H35 at 10 Torr. Here, $\Delta k_{q,el}$ is always positive, and $\Delta k_{q,at}$ usually is negative for high-energy photons. As shown in Fig. 8, these two terms can compensate, i.e., add up to near zero, at a very low ionization level (about 6% for H15, and 4% for H35). Here a 780-nm, three-cycle (FWHM) laser is applied. More discussions can be found in the works of Murnane and Kapteyn [41–43]. On the other hand, gas pressure also induces laser defocusing and blue shift, thus changing the geometric phase mismatch $\Delta k_{q,geo}$ in Eq. (B1) and $K_{q,dip}$ in Eq. (B3). It is difficult to quantify the variations of these values since the laser field undergoes complicated spatial and temporal variation in the medium. In the following, we only illustrate the effect of laser defocusing by changing the confocal parameter b for a Gaussian beam.

We first give a rough estimate of phase mismatch caused by the pressure, i.e., $\Delta k_{q,el} + \Delta k_{q,at}$, and $\Delta k_{q,geo} - K_{q,dip}$, due to the laser defocusing. For the tight-focusing Gaussian beam, the ionization level (in the end of the laser pulse) is about 12%, thus the values of $\Delta k_{q,el} + \Delta k_{q,at}$ are about 0.5 and 2 mm^{-1} at 10 Torr for H15 and H35, respectively (see Fig. 8). These values increase to 4 and 16 mm^{-1} at 80 Torr. On the other hand, pressure could induce laser defocusing, i.e., making the confocal parameter b smaller. In Table I, we show $\Delta k_{q,geo}$ and $K_{q,dip}$ as b changes to 3 mm. We can see, at 10 Torr, the phase mismatch caused by the laser focusing is dominant, and then becomes comparable to $\Delta k_{q,el} + \Delta k_{q,at}$ at 80 Torr. For Type-1 Bessel and Gaussian beams, the geometric phase and induced dipole phase between the two beams have been shown to be quite different (see Fig. 4). With the increase in pressure, their differences still prevail, so the harmonic spatial distributions

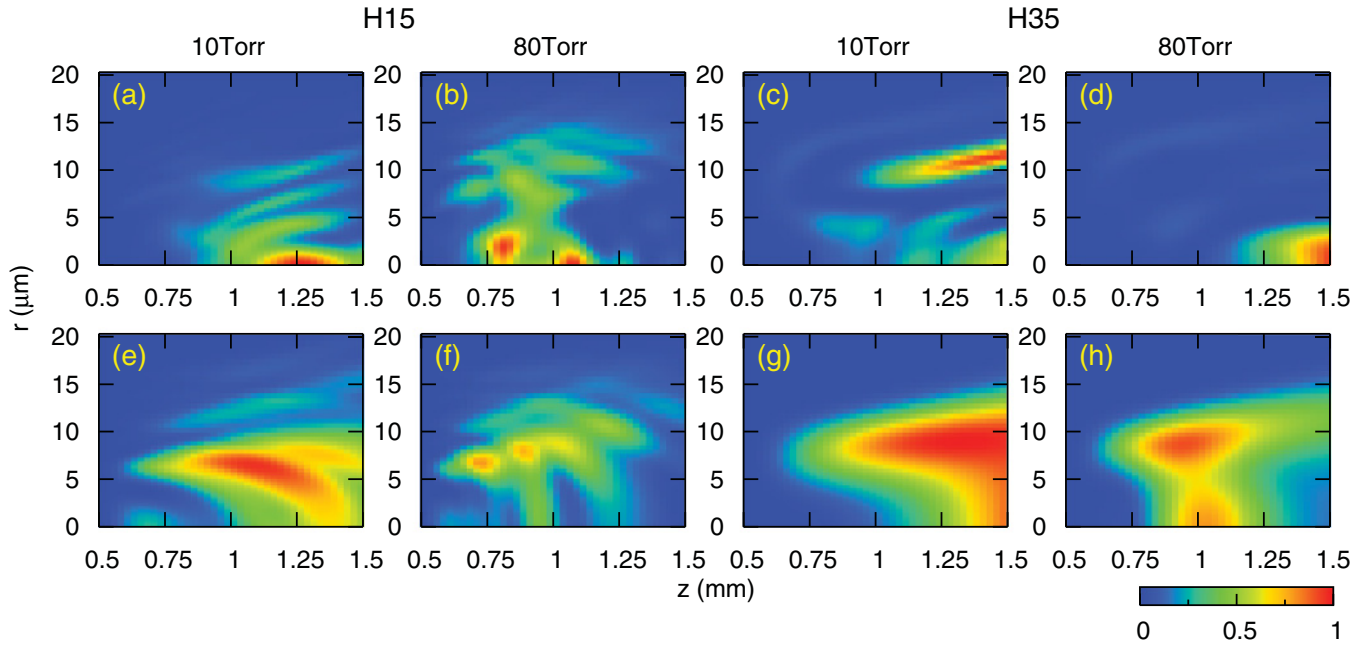


FIG. 9. (Color online) Spatial distributions (normalized) of the harmonic intensity under different pressures (10 and 80 Torr) using tight-focusing laser beams. $z_0 = 1$ mm (as can be read from the z coordinate). The gas jet is 1-mm wide, and harmonic order is indicated. Upper row: Type-1 Bessel beam; lower row: Gaussian beam ($w_0 = 25 \mu\text{m}$).

for the two beams behave differently at higher pressure as well. Figure 9 shows the spatial harmonic emissions for Type-1 Bessel and Gaussian beams at two pressures, and they are quite different for the two tightly focused beams.

We carry out a similar analysis for the loosely focused laser beams. The ionization level is found to be about 15% for the loose-focusing Gaussian beam, so the values of $\Delta k_{q,el} + \Delta k_{q,at}$ are about 1 and 3.5 mm^{-1} at 10 Torr for H15

and H35, respectively (see Fig. 8). These values increase to 8 and 28 mm^{-1} at 80 Torr. In Table I, changing b to 15 mm for the Gaussian beam does not change the phase mismatch much. $\Delta k_{q,geo} - K_{q,dip}$ is comparable with $\Delta k_{q,el} + \Delta k_{q,at}$ at 10 Torr, and then $\Delta k_{q,el} + \Delta k_{q,at}$ becomes dominant as the pressure is increased. Figure 10 shows that the spatial harmonic emissions for Type-2 Bessel and Gaussian beams are similar even at moderate pressures.

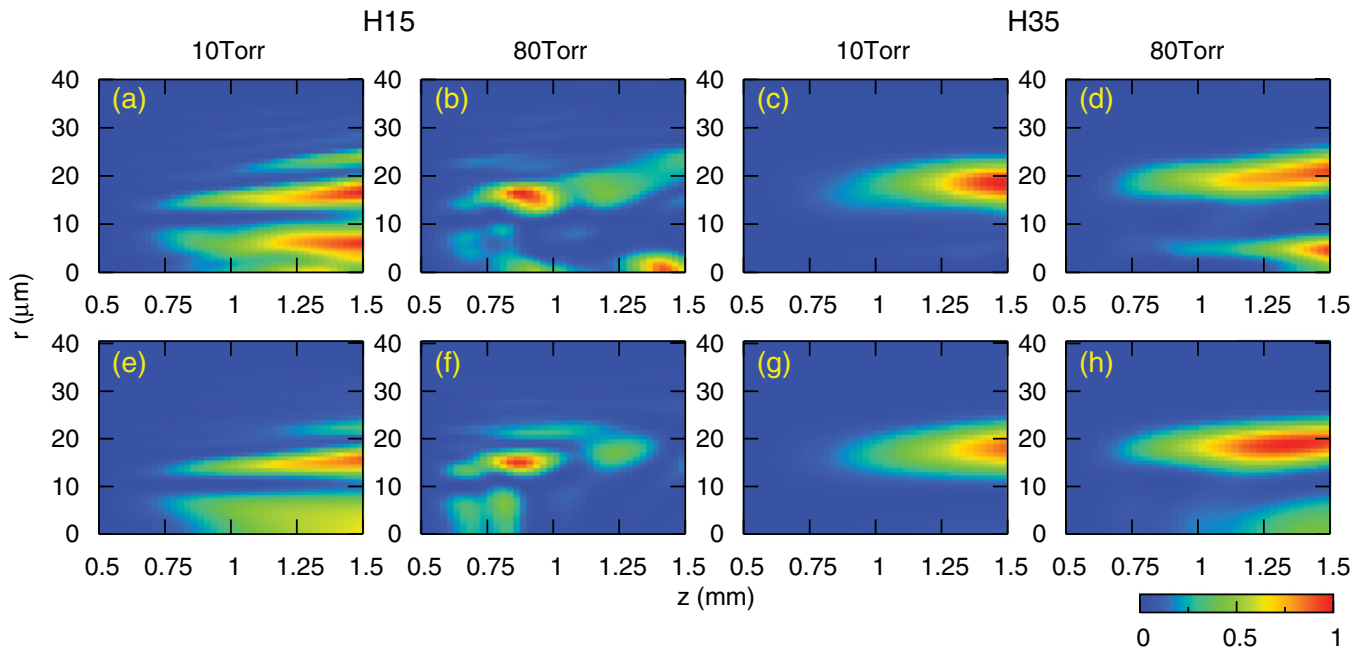


FIG. 10. (Color online) Same as Fig. 9, except for the loose-focusing laser beams. Upper row: Type-2 Bessel beam; lower row: Gaussian beam ($w_0 = 50 \mu\text{m}$).

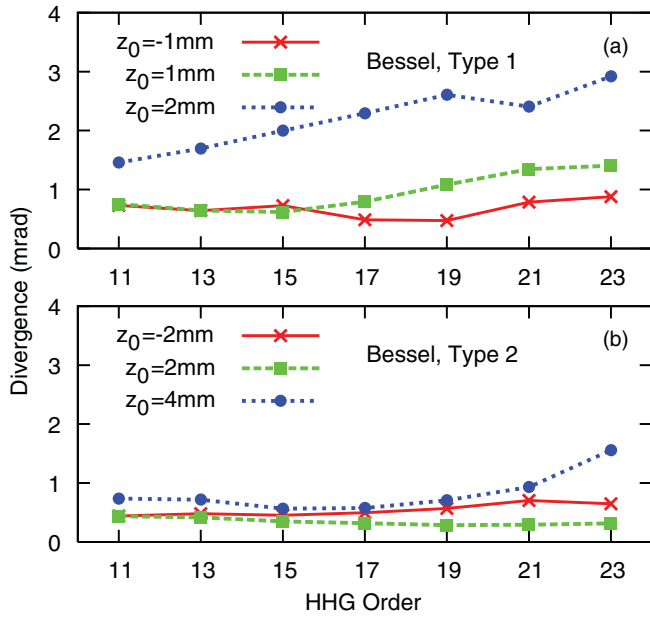


FIG. 11. (Color online) Divergence of harmonic beam vs harmonic order, for different gas-jet positions, z_0 . Gas pressure: 30 Torr.

D. Divergence of harmonics

We define the divergence angle of a harmonic as follows [44]:

$$\bar{\theta}_q = \frac{\int_0^{\theta_{\max}} \theta I_q(\theta) d\theta}{\int_0^{\theta_{\max}} I_q(\theta) d\theta}, \quad (6)$$

where θ is the divergence angle, $I_q(\theta)$ is the harmonic intensity in the far field, and θ_{\max} is the maximal acceptance angle of the experimental apparatus. We plot the divergence angle vs harmonic order for the two types of Bessel beams in Fig. 11 at each harmonic peak. For the Type-1 Bessel beam, the divergence angle for the gas jet near the laser focus ($z_0 = -1$ and 1 mm) is small, but it suddenly jumps to a big value at $z_0 = 2$ mm. This behavior is consistent with the results reported in Nisoli *et al.* for Ne [23]. For the Type-2 Bessel, there are no divergence jumps when varying the gas-jet position z_0 from -2 to 4 mm. We can also see that the loosely focused laser beam tends to generate low-divergence harmonics.

IV. SUMMARY

In this paper, we examined the generation of harmonics in the gas medium for incident intense lasers that have Gaussian or truncated Bessel spatial profiles. We investigated how the generated harmonic emissions (with the inclusion of a propagation effect) depend on the gas-jet position and gas pressure for tightly and loosely focused Bessel and Gaussian beams. First we simulated the HHG spectra of Ar reported in Wörner *et al.* [26] using the 780-nm few-cycle pulses. We concluded that we are unable to reproduce the deep and broad Cooper minimum in the observed HHG spectra of Ar, whether we assume that the spatial profile was a truncated Bessel beam or a Gaussian beam. However, our simulation was able to reproduce the observed HHG spectra of Ar generated using 1800-nm lasers in Shiner *et al.* [27]. We suggested that

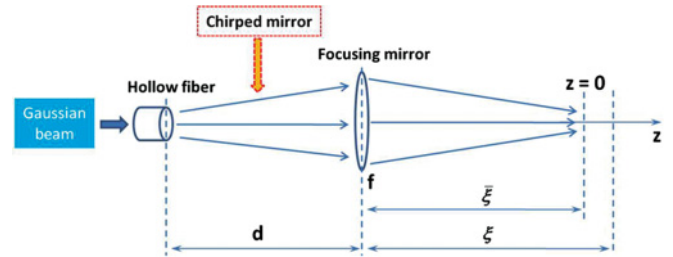


FIG. 12. (Color online) Sketch of the experimental setup for Type-1 Bessel beam generation [23].

additional experiments might be needed to clarify the existing discrepancy for the 780-nm data.

We also analyzed phase-matching conditions for tightly and loosely focused Bessel and Gaussian beams, and varied the gas-jet position and gas pressure. We demonstrated that for loosely focused Bessel or Gaussian beams, the harmonic growth maps were very similar, thus resulting in nearly identical harmonic spectra. For tightly focused beams, the harmonic growth maps were different for Bessel and Gaussian beams, and the resulting HHG spectra differed from each other as well. At higher pressure and/or intensity, phase-matching analysis is complicated due to laser defocusing and blue shift, as the laser intensity changes in the gas medium. To probe an atomic or molecular electronic structure using HHG, harmonics generated from loosely focused beams are preferable since the spectra would be less sensitive to gas-jet location and other experimental parameters. For tightly focused beams, the harmonic spectra are very sensitive to experimental conditions such that the comparison of theoretical simulation with experiment is less straightforward, since experimental parameters are not all generally well specified.

ACKNOWLEDGMENTS

This work was supported in part by the Chemical Sciences, Geosciences and Biosciences Division, Office of Basic Energy Sciences, Office of Science, US Department of Energy. C.J. also thanks Dr. Hans J. Wörner for valuable communications.

APPENDIX A: TRUNCATED BESSEL BEAMS

For an axial-symmetric lenslike system, the complex electric field on the output plane is related to the one on the input plane by an $ABCD$ ray matrix [45,46]. Let the laser electric field on the input plane (the exit plane of a hollow-core fiber) be given by $E(\rho) = E_0 J_0(2.405\rho/a)$ with $\rho \leq a$, where ρ is the radial coordinate, E_0 is the on-axis peak electric field, a is the capillary radius, and J_0 is the zero-order Bessel function of the first kind. The transverse electric field on the output plane, according to the diffraction theory in the paraxial approximation, is

$$E_{\text{TB}}(\xi, r) = E_0 \frac{-ik}{B(\xi)} \exp \left\{ ik \left[L + \xi + \frac{Dr^2}{2B(\xi)} \right] \right\} \times \int_0^a J_0 \left(2.405 \frac{\rho}{a} \right) J_0 \left[\frac{kr\rho}{B(\xi)} \right] \exp \left[\frac{ikA(\xi)}{2B(\xi)} \rho^2 \right] \rho d\rho, \quad (\text{A1})$$

where $k = 2\pi/\lambda_1$, and λ_1 is the central laser wavelength. The meanings of the parameters in the equation will be defined explicitly below. We note that the integral in Eq. (A1) becomes indeterminate if $B(\xi = \bar{\xi}) = 0$, where $\xi = \bar{\xi}$ is also the location of the focus plane. As discussed in Ref. [46], the electric field at $\bar{\xi}$ can be written as

$$E_{\text{TB}}(\bar{\xi}, r) = \frac{E_0}{A} \exp \left[ik \left(L + \bar{\xi} + \frac{Cr^2}{2A} \right) \right] J_0 \left(2.405 \frac{r}{aA} \right). \quad (\text{A2})$$

For a lossless system, $AD - BC = 1$. In the following, we will show two truncated Bessel (TB) beams from the different optical systems, which have been used by Nisoli *et al.* [23] and Wörner *et al.* [26], respectively.

1. Type-1 Bessel beam: Tightly focused beam

In the experiment of Nisoli *et al.* [23], the setup of the optical system is depicted in Fig. 12. The radius of the capillary is $a = 0.25$ mm, and the focal length of the focus mirror is $f = 250$ mm. The ξ and the focus plane $\bar{\xi}$ are sketched in the figure. The laser pulse emerging from the hollow-core fiber propagates in free space for a distance $d = 2000$ mm [or L in Eq. (A1)] to the focusing mirror, where it further propagates for a distance ξ after the mirror to the output plane. The laser pulse is also compressed by chirped mirrors, but they are not included in the $ABCD$ matrix. For this optical system, the $ABCD$ matrix is

$$\begin{aligned} A(\xi) &= 1 - \xi/f, & B(\xi) &= d + \xi(1 - d/f), & C &= -1/f, \\ D &= 1 - d/f. \end{aligned} \quad (\text{A3})$$

The TB beam constructed by Eq. (A3) is called the Type-1 Bessel beam in this paper. We plot the intensity $|E_{\text{TB}}|^2$ and the phase ϕ_{TB} (red solid lines) as a function of z for $r = 0$ (on-axis) in Figs. 13(a) and 13(b), respectively. Here the coordinate ξ has been replaced by $z = \xi - \bar{\xi}$ for convenience, and the phase ϕ_{TB} is set as 0 at $z = 0$ and $r = 0$ (focusing point). In the present case, $\bar{\xi} > f$, where $B(\bar{\xi}) = 0$ with B defined in Eq. (A3). The laser wavelength $\lambda_1 = 780$ nm, and the laser intensity at the focus is 3×10^{14} W/cm². For comparison, we fix the laser intensity at the focus and plot the intensity and phase (dashed lines) of a Gaussian beam with the beam waist $w_0 = 25$ μm in Figs. 13(a) and 13(b), respectively. In Fig. 13(c), we plot the spatial distribution of the laser intensity for the TB beam. We also introduce the pulse energy W_{pulse} for the laser beam,

$$W_{\text{pulse}} = \int \int I(r, z, t) 2\pi r dr dt, \quad (\text{A4})$$

where $I(r, z, t)$ is the spatial- and temporal-dependent laser intensity (assuming cylindrical symmetry). For a Gaussian beam, the explicit expression of $I(r, z, t)$ in Eq. (A4) can be found in Ref. [14]; we then have an analytical expression for the pulse energy,

$$W_{\text{pulse}} = I_0 \frac{\pi w_0^2}{2} \tau_p \sqrt{\frac{\pi}{4 \ln 2}}, \quad (\text{A5})$$

where I_0 is the laser peak intensity at the focus, τ_p is the pulse duration (FWHM), and w_0 is the beam waist. We choose τ_p

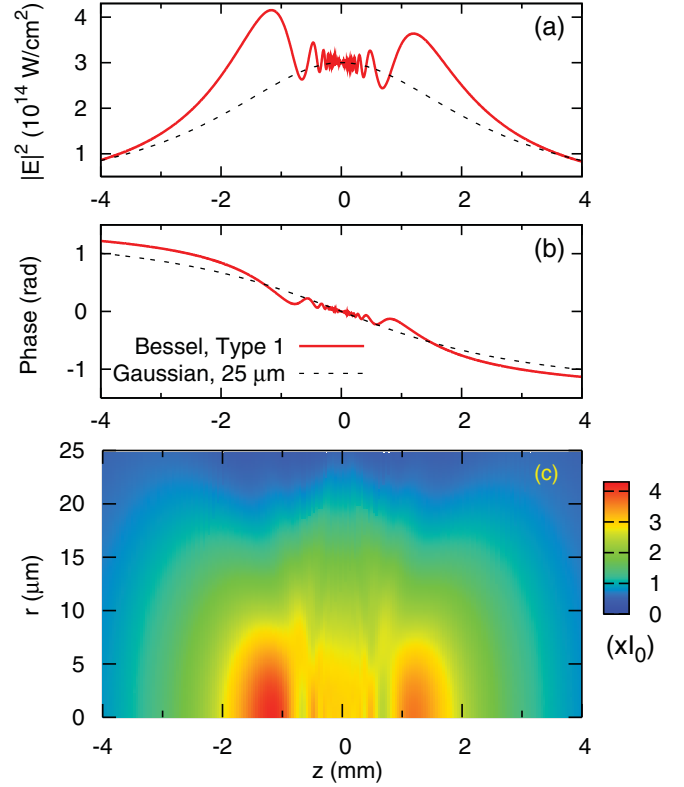


FIG. 13. (Color online) (a) On-axis laser intensity and (b) phase as a function of propagation distance z : Type-1 Bessel (solid lines) vs Gaussian ($w_0 = 25$ μm , dashed lines). (c) Spatial intensity distribution (where I_0 is in the units of 10^{14} W/cm²) of the Type-1 Bessel beam. The laser intensity at the focus is 3×10^{14} W/cm².

to be three cycles (7.8 fs), then W_{pulse} obtained by Eq. (A5) is 24.45 μJ for the Gaussian beam in Fig. 13. And W_{pulse} is 27.24 μJ for the Type-1 Bessel beam in Fig. 13 calculated using Eq. (A4) numerically.

2. Type-2 Bessel beam: Loosely focused beam

For the experiment of Wörner *et al.* [26], the setup is depicted in Fig. 14. The hollow-core fiber (HCF) is similar to that of Nisoli *et al.* [23]. The beam that comes out of the HCF

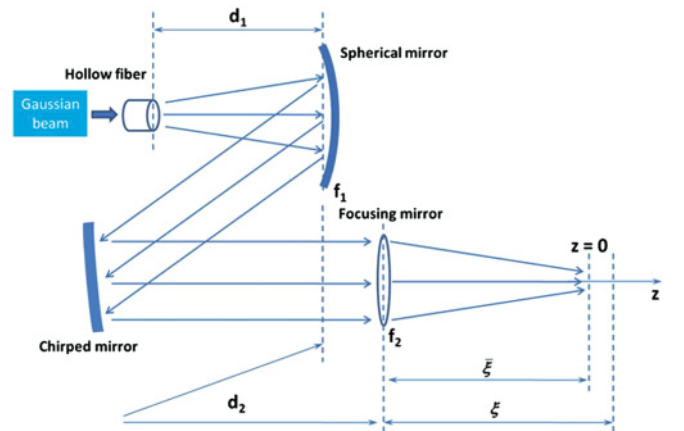


FIG. 14. (Color online) Sketch of the experimental setup used by Wörner *et al.* [26] for Type-2 Bessel beam generation.

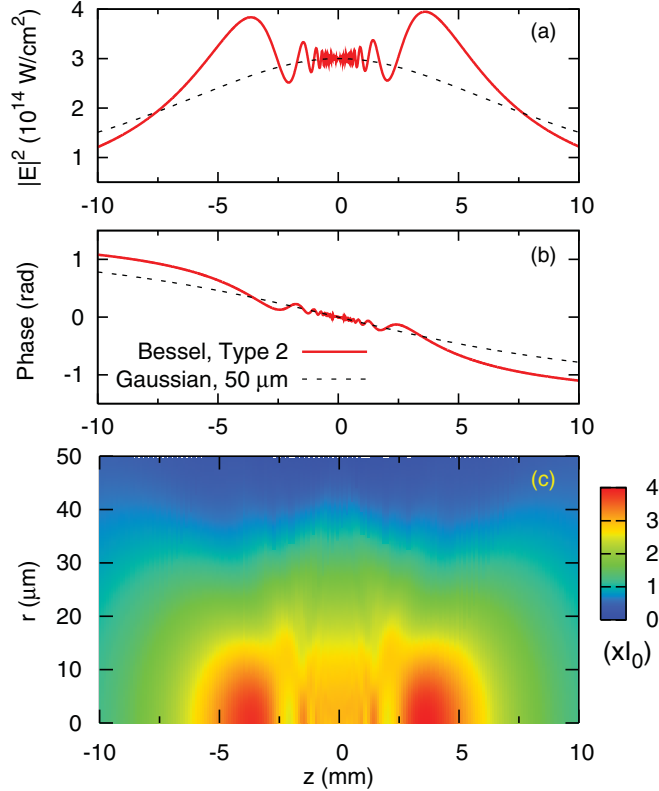


FIG. 15. (Color online) Same as Fig. 13, except for loosely focused Type-2 Bessel and Gaussian ($w_0 = 50 \mu\text{m}$) beams.

(with radius $a = 0.125 \text{ mm}$) is divergent and it is recollimated by a spherical mirror (with focal length $f_1 = 1000 \text{ mm}$) placed 1 m after the output of the HCF ($d_1 = 1000 \text{ mm}$). The beam is then reflected eight times on chirped mirrors and propagated a distance of 2 m from the spherical mirror ($d_2 = 2000 \text{ mm}$) until it reaches a focusing mirror (focal length $f_2 = 500 \text{ mm}$). It further propagates through a distance ξ after the mirror to the output plane. L in Eq. (A1) is equal to $d_1 + d_2$. We then write the $ABCD$ matrix for this optical system without considering the chirped mirrors:

$$\begin{aligned}
 A(\xi) &= \left(1 - \frac{d_2}{f_1}\right) \left(1 - \frac{\xi}{f_2}\right) - \frac{\xi}{f_1}, \\
 B(\xi) &= \left(d_1 + d_2 - \frac{d_1 d_2}{f_1}\right) \left(1 - \frac{\xi}{f_2}\right) - \xi \left(\frac{d_1}{f_1} - 1\right), \\
 C &= -\frac{1}{f_1} - \frac{1}{f_2} + \frac{d_2}{f_1 f_2}, \\
 D &= -\frac{d_1}{f_2} + \left(1 - \frac{d_1}{f_1}\right) \left(1 + \frac{d_2}{f_2}\right).
 \end{aligned} \tag{A6}$$

To have the collimated laser beam before the focusing mirror f_2 requires $d_1 = f_1$, i.e., the output of the HCF is put at the focal plane of the spherical mirror f_1 . In this case, $\xi = f_2$. The TB beam constructed by Eq. (A6) is called the Type-2 Bessel beam in this paper. Similar to Fig. 13, we plot the on-axis intensity $|E_{\text{TB}}|^2$ and the phase ϕ_{TB} (red solid lines) as a function of z and the spatial distribution of intensity in Fig. 15. In Figs. 15(a) and 15(b), we also plot the on-axis intensity and phase (dashed lines) of a Gaussian beam with

the beam waist $w_0 = 50 \mu\text{m}$. The same laser wavelength and intensity (at the focus) are applied. Similarly, E_{pulse} is $82.37 \mu\text{J}$ for the Type-2 Bessel beam, and $97.82 \mu\text{J}$ for the Gaussian beam in Fig. 15.

APPENDIX B: PHASE-MATCHING FACTORS

Generally, phase matching is the matching of the phase front of the generated harmonic field to the phase front of the fundamental laser field. In a strong-field interaction, phase matching could have complicated spatial and temporal dependence due to the variation of the laser intensity. The phase-matching relation for the q th harmonic has been given in Eq. (3) as consisting of four terms [5,35–38]. Each dispersion term will be discussed in the following.

1. Geometric dispersion

The phase mismatch introduced by laser focusing is

$$\Delta k_{q,\text{geo}}(r,z) = \delta k_{q,\text{geo}}(r,z) - q \delta k_{1,\text{geo}}(r,z). \tag{B1}$$

We take a Gaussian beam for example. Consider on-axis ($r = 0$) phase matching only, and assume that the fundamental laser and harmonic fields have the same geometrical phase. Then, $\Delta k_{q,\text{geo}}$ can be written as

$$\begin{aligned}
 \Delta k_{q,\text{geo}}(0,z) &\approx -(q-1) \delta k_{1,\text{geo}}(0,z) \\
 &= \frac{2}{b} (q-1) \frac{1}{1 + (2z/b)^2},
 \end{aligned} \tag{B2}$$

where $b = 2\pi w_0^2/\lambda_1$ is the confocal parameter.

2. Induced dipole phase

In the strong-field regime, the induced dipole phase strongly depends on the laser intensity, so the spatial variation of the focused laser beam results in longitudinal and transverse gradients of this phase. The phase mismatch is

$$K_{q,\text{dip}}(r,z) = \nabla \varphi_{q,\text{dip}}(r,z). \tag{B3}$$

Here this intrinsic dipole phase $\varphi_{q,\text{dip}}$ is the action accumulated by an electron during its excursion in the external field along the trajectory leading to the emission of the q th harmonic. It can be expressed as

$$\varphi_{q,\text{dip}}(r,z) = -\alpha_i^q I(r,z), \tag{B4}$$

where $I(r,z)$ is the instantaneous laser intensity. The proportional constant $\alpha_{i=S,L}^q$ depends on short (S) or long (L) trajectories. When the harmonics are in the plateau region, $\alpha_{i=S}^q \approx 1 \times 10^{-14} \text{ rad cm}^2/\text{W}$ and $\alpha_{i=L}^q \approx 24 \times 10^{-14} \text{ rad cm}^2/\text{W}$ [47–50]. In the cutoff region, these two trajectories merge into one trajectory, and $\alpha_{i=S,L}^q \approx 13.7 \times 10^{-14} \text{ rad cm}^2/\text{W}$. We only consider the on-axis phase mismatch of a Gaussian beam for simplicity. It can be written as follows:

$$\begin{aligned}
 \frac{\partial \varphi_{q,\text{dip}}(0,z)}{\partial z} &= -\alpha_i^q \frac{\partial I(0,z)}{\partial z} \\
 &= \frac{8z}{b^2} \frac{1}{[1 + (2z/b)^2]^2} \alpha_i^q I_0,
 \end{aligned} \tag{B5}$$

where I_0 is the peak intensity at the laser focus.

3. Plasma (electronic) dispersion

The first step of harmonic generation is tunneling ionization of an atom. Only a small portion of free electrons returns to recombine with the parent ion. The electrons in the medium create a plasma surrounding which could modify the refractive index. The phase mismatch due to the free electrons (or plasma) is

$$\begin{aligned}\Delta k_{q,el}(r,z,t) &= \delta k_{q,el}(r,z,t) - q\delta k_{1,el}(r,z,t) \\ &\approx \frac{e^2 n_e(r,z,t)}{4\pi\epsilon_0 m_e c^2} q\lambda_1 \\ &= qr_0 n_e(r,z,t)\lambda_1,\end{aligned}\quad (\text{B6})$$

where $n_e(r,z,t)$ is the electron density, and e , m_e , and r_0 are the charge, mass, and classical radius of an electron, respectively. Here the free-electron dispersion for the harmonic field is neglected because the frequencies of high harmonics are much higher than the plasma frequency. Note that this term is proportional to the harmonic order q .

4. Atomic dispersion

The phase mismatch due to neutral atom dispersion is

$$\begin{aligned}\Delta k_{q,at}(r,z,t) &= \delta k_{q,at}(r,z,t) - q\delta k_{1,at}(r,z,t) \\ &\approx -\frac{n_0(r,z,t)\pi\alpha_1}{\lambda_q} - n_0(r,z,t)r_0\lambda_q f_1,\end{aligned}\quad (\text{B7})$$

where $n_0(r,z,t)$ is the atom density, $\lambda_q = \lambda_1/q$ is the wavelength of the q th harmonic, and α_1 is the atomic polarizability at the fundamental wavelength λ_1 . Here, f_1 is the real part of the atomic scattering factor, $f = f_1 + if_2$ [51,52], at the harmonic wavelength λ_q . And the imaginary part f_2 is related to the absorption length L_{abs} by $L_{\text{abs}}^{-1} = 2r_0\lambda_q n_0(r,z,t)f_2$. In the propagation calculation [15], the spatial and temporal variation of the harmonic dispersion is ignored, so in the analysis of $\Delta k_{q,at}(r,z,t)$, we treat $n_0(r,z,t)$ in the second term of Eq. (B7) as a constant. The Kerr nonlinearity [15] depending on the laser intensity is the third-order effect and it is not included in the present phase-mismatch analysis.

-
- [1] A. Rundquist, C. G. Durfee III, Z. Chang, C. Herne, S. Backus, M. M. Murnane, and H. C. Kapteyn, *Science* **280**, 1412 (1998).
- [2] R. A. Bartels, A. Paul, H. Green, H. C. Kapteyn, M. M. Murnane, S. Backus, I. P. Christov, Y. Liu, D. Attwood, and C. Jacobsen, *Science* **297**, 376 (2002).
- [3] F. Krausz and M. Ivanov, *Rev. Mod. Phys.* **81**, 163 (2009).
- [4] P. Agostini and L. F. DiMauro, *Rep. Prog. Phys.* **67**, 813 (2004).
- [5] M. B. Gaarde, J. L. Tate, and K. J. Schafer, *J. Phys. B* **41**, 132001 (2008).
- [6] J. L. Krause, K. J. Schafer, and K. C. Kulander, *Phys. Rev. Lett.* **68**, 3535 (1992).
- [7] P. B. Corkum, *Phys. Rev. Lett.* **71**, 1994 (1993).
- [8] M. Lewenstein, Ph. Balcou, M. Yu. Ivanov, A. L'Huillier, and P. B. Corkum, *Phys. Rev. A* **49**, 2117 (1994).
- [9] C. D. Lin, A. T. Le, Z. Chen, T. Morishita, and R. R. Lucchese, *J. Phys. B* **43**, 122001 (2010).
- [10] T. Morishita, A. T. Le, Z. Chen, and C. D. Lin, *Phys. Rev. Lett.* **100**, 013903 (2008).
- [11] A. T. Le, R. R. Lucchese, S. Tonzani, T. Morishita, and C. D. Lin, *Phys. Rev. A* **80**, 013401 (2009).
- [12] M. V. Frolov, N. L. Manakov, T. S. Sarantseva, and A. F. Starace, *J. Phys. B* **42**, 035601 (2009).
- [13] M. V. Frolov, N. L. Manakov, T. S. Sarantseva, and A. F. Starace, *Phys. Rev. A* **83**, 043416 (2011).
- [14] C. Jin, A. T. Le, and C. D. Lin, *Phys. Rev. A* **79**, 053413 (2009).
- [15] C. Jin, A. T. Le, and C. D. Lin, *Phys. Rev. A* **83**, 023411 (2011).
- [16] C. Jin, H. J. Wörner, V. Tosa, A. T. Le, J. B. Bertrand, R. R. Lucchese, P. B. Corkum, D. M. Villeneuve, and C. D. Lin, *J. Phys. B* **44**, 095601 (2011).
- [17] C. Jin, J. B. Bertrand, R. R. Lucchese, H. J. Wörner, P. B. Corkum, D. M. Villeneuve, A. T. Le, and C. D. Lin, *Phys. Rev. A* **85**, 013405 (2012).
- [18] C. Jin, A. T. Le, and C. D. Lin, *Phys. Rev. A* **83**, 053409 (2011).
- [19] C. Trallero-Herrero, C. Jin, B. E. Schmidt, A. D. Shiner, J.-C. Kieffer, P. B. Corkum, D. M. Villeneuve, C. D. Lin, F. Légaré, and A. T. Le, *J. Phys. B* **45**, 011001 (2012).
- [20] C. Jin, A. T. Le, C. A. Trallero-Herrero, and C. D. Lin, *Phys. Rev. A* **84**, 043411 (2011).
- [21] G. Wang, C. Jin, A. T. Le, and C. D. Lin, *Phys. Rev. A* **84**, 053404 (2011).
- [22] M. Nisoli, S. De Silvestri, and O. Svelto, *Appl. Phys. Lett.* **68**, 2793 (1996).
- [23] M. Nisoli *et al.*, *Phys. Rev. Lett.* **88**, 033902 (2002).
- [24] M. Nisoli *et al.*, *Appl. Phys. B* **74**, s11 (2002).
- [25] H.-C. Bandulet, D. Comtois, A. D. Shiner, C. Trallero-Herrero, N. Kajumba, T. Ozaki, P. B. Corkum, D. M. Villeneuve, J.-C. Kieffer, and F. Légaré, *J. Phys. B* **41**, 245602 (2008).
- [26] H. J. Wörner, H. Niikura, J. B. Bertrand, P. B. Corkum, and D. M. Villeneuve, *Phys. Rev. Lett.* **102**, 103901 (2009).
- [27] A. D. Shiner, B. E. Schmidt, C. Trallero-Herrero, H. J. Wörner, S. Patchkovskii, P. B. Corkum, J.-C. Kieffer, F. Légaré, and D. M. Villeneuve, *Nature Phys.* **7**, 464 (2011).
- [28] J. A. R. Samson and W. C. Stolte, *J. Electron Spectrosc. Relat. Phenom.* **123**, 265 (2002).
- [29] S. Minemoto, T. Umegaki, Y. Oguchi, T. Morishita, A. T. Le, S. Watanabe, and H. Sakai, *Phys. Rev. A* **78**, 061402 (2008).
- [30] E. J. Takahashi, T. Kanai, Y. Nabekawa, and K. Midorikawa, *Appl. Phys. Lett.* **93**, 041111 (2008).
- [31] P. Colosimo *et al.*, *Nature Phys.* **4**, 386 (2008).
- [32] J. P. Farrell, L. S. Spector, B. K. McFarland, P. H. Bucksbaum, M. Gühr, M. B. Gaarde, and K. J. Schafer, *Phys. Rev. A* **83**, 023420 (2011).
- [33] J. Higué *et al.*, *Phys. Rev. A* **83**, 053401 (2011).
- [34] H. G. Müller, *Phys. Rev. A* **60**, 1341 (1999).
- [35] T. Pfeifer, C. Spielmann, and G. Gerber, *Rep. Prog. Phys.* **69**, 443 (2006).
- [36] C. Winterfeldt, C. Spielmann, and G. Gerber, *Rev. Mod. Phys.* **80**, 117 (2008).
- [37] P. Balcou, P. Salières, A. L'Huillier, and M. Lewenstein, *Phys. Rev. A* **55**, 3204 (1997).
- [38] H. Dachraoui, T. Auguste, A. Helmstedt, P. Bartz, M. Michelswirth, N. Mueller, W. Pfeiffer, P. Salières, and U. Heinzmann, *J. Phys. B* **42**, 175402 (2009).
- [39] L. E. Chipperfield, P. L. Knight, J. W. G. Tisch, and J. P. Marangos, *Opt. Commun.* **264**, 494 (2006).

- [40] S. Kazamias, S. Daboussi, O. Guilbaud, K. Cassou, D. Ros, B. Cros, and G. Maynard, *Phys. Rev. A* **83**, 063405 (2011).
- [41] T. Popmintchev, M.-C. Chen, O. Cohen, M. E. Grisham, J. J. Rocca, M. M. Murnane, and H. C. Kapteyn, *Opt. Lett.* **33**, 2128 (2008).
- [42] T. Popmintchev, M.-C. Chen, A. Bahabad, M. Gerrity, P. Sidorenko, O. Cohen, I. P. Christov, M. M. Murnane, and H. C. Kapteyn, *Proc. Natl. Acad. Sci. USA* **106**, 10516 (2009).
- [43] M.-C. Chen, P. Arpin, T. Popmintchev, M. Gerrity, B. Zhang, M. Seaberg, D. Popmintchev, M. M. Murnane, and H. C. Kapteyn, *Phys. Rev. Lett.* **105**, 173901 (2010).
- [44] C. Altucci *et al.*, *Phys. Rev. A* **68**, 033806 (2003).
- [45] S. A. J. Collins, *J. Opt. Soc. Am. A* **60**, 1168 (1970).
- [46] A. Yariv, *Opt. Lett.* **19**, 1607 (1994).
- [47] M. Lewenstein, P. Salières, and A. L’Huillier, *Phys. Rev. A* **52**, 4747 (1995).
- [48] Ph. Balcou, A. S. Dederichs, M. B. Gaarde, and A. L’Huillier, *J. Phys. B* **32**, 2973 (1999).
- [49] M. B. Gaarde, F. Salin, E. Constant, Ph. Balcou, K. J. Schafer, K. C. Kulander, and A. L’Huillier, *Phys. Rev. A* **59**, 1367 (1999).
- [50] M. B. Gaarde and K. J. Schafer, *Phys. Rev. A* **65**, 031406 (2002).
- [51] C. T. Chantler, K. Olsen, R. A. Dragoset, J. Chang, A. R. Kishore, S. A. Kotochigova, and D. S. Zucker, *X-ray Form Factor, Attenuation and Scattering Tables*, Version 2.1 (National Institute of Standards and Technology, Gaithersburg, MD, 2005); [<http://physics.nist.gov/ffast>].
- [52] B. L. Henke, E. M. Gullikson, and J. C. Davis, *At. Data Nucl. Data Tables* **54**, 181 (1993).